Journal of Power Sources 194 (2009) 763–773

Contents lists available at ScienceDirect

Journal of Power Sources

journal homepage: www.elsevier.com/locate/jpowsour

Numerical modeling and analysis of micro-porous layer effects in polymer electrolyte fuel cells

Kyungmun Kang, Hyunchul Ju*

School of Mechanical Engineering, Inha University, 253 Yonghyun-Dong, Nam-Gu, Incheon 402-751, Republic of Korea

ARTICLE INFO

Article history:
Received 21 February 2009
Received in revised form 15 April 2009
Accepted 25 May 2009
Available online 9 June 2009

Keywords:
Fuel cell
Micro-porous layer
Two-phase transport
Flooding
Gas diffusion layer

ABSTRACT

It is well known that a micro-porous layer (MPL) plays a crucial role in the water management of polymer electrolyte fuel cells (PEFCs), and thereby, significantly stabilizes and improves cell performance. To ascertain the exact roles of MPLs, a numerical MPL model is developed in this study and incorporated with comprehensive, multi-dimensional, multi-phase fuel-cell models that have been devised earlier. The effects of different porous properties and liquid-entry pressures between an MPL and a gas diffusion layer (GDL) are examined via fully three-dimensional numerical simulations. First, when the differences in pore properties and wettability between the MPL and GDL are taken into account but the difference in the entry pressures is ignored, the numerical MPL model captures a discontinuity in liquid saturation at the GDL|MPL interface. The simulation does not, however, capture the beneficial effects of an MPL on cell performance, predicting even lower performance than in the case of no MPL. On the other hand, when a high liquid-entry pressure in an MPL is additionally considered, the numerical MPL model predicts a liquid-free MPL and successfully demonstrates the phenomenon that the high liquid-entry pressure of the MPL prevents any liquid water from entering the MPL. Consequently, it is found from the simulation results that a liquid-free MPL significantly enhances the back-flow of water across the membrane into the anode, which, in turn, helps to avoid membrane dehydration and alleviate the level of GDL flooding. As a result, the model successfully reports the beneficial effects of MPLs on PEFC performance and predicts higher performance in the presence of MPLs (e.g., an increase of 67 mV at 1.5 A cm^{-2}). This study provides a fundamental explanation of the function of MPLs and quantifies the influence of their porous properties and the liquid-entry pressure on water transport and cell performance.

1. Introduction

It has been widely observed experimentally that the performance of polymer electrolyte fuel cells (PEFCs) is significantly stabilized and improved by adding a micro-porous layer (MPL) to the interface between a gas diffusion layer (GDL) and a catalyst coated membrane (CCM) [1–8]. Therefore, the choice of the proper GDL–MPL combination is critical to achieve favorable PEFC performance and durability. An MPL is made of a mixture of carbon black powder and a hydrophobic agent, usually polytetrafluoroethylene (PTFE), yielding a relatively finer pore structure and a highly hydrophobic feature than GDLs. While the use of MPLs in PEFCs has been a common practice due to the resulting dramatic effects, the exact role of an MPL is uncertain due to several inherent difficulties and, in particular, the complicated multi-phase transport and flooding behaviour between the MPL and its neighboring components. These components may be either GDLs or catalyst layers (CLs), in of which the morphological structures of the pores and the wetting characteristics are all different from those of the MPL. Therefore, recently published studies on MPLs focus mostly on a more precise investigation and analysis of the role of the MPL on water transport and the relevant PEFC performance.

The effects of MPL composition, morphology, and wettability on reactant gases and product water transport in PEFCs have been experimentally investigated [9–15]. Wang et al. [9,10] observed the influence on PEFC performance of carbon powders that were employed to fabricate MPLs. They reported the dual role of the GDL–MPL pore structure in the transport of reactant gases and product water, where the hydrophobic pores in the GDL and MPL facilitate gas transport whereas the hydrophilic pores allow a pathway for liquid transport. They concluded that an appropriate combination of hydrophilic and hydrophobic pores is crucial for optimizing a GDL–MPL component for the proper water management of PEFCs. Chen et al. [11] focused on MPL preparation methods, i.e., conventional wet-layer and novel dry-layer methods. Given the differences in the surface morphology and pore-size distribution between GDLs that use either dry-layer or wet-layer MPLs, they demonstrated that the former MPLs exhibit better PEFC

* Corresponding author. Tel.: +82 32 860 7312; fax: +82 32 868 1716.
E-mail address: hcju@inha.ac.kr (H. Ju).

0378-7753/$ – see front matter © 2009 Elsevier B.V. All rights reserved.
doi:10.1016/j.jpowsour.2009.05.046

Nomenclature

a	water activity or effective catalyst area per unit of total volume ($m^2\ m^{-3}$)
A	area (m^2)
C_P	specific heat ($kJ\ kg^{-1}\ K^{-1}$)
C	molar concentration ($mol\ m^{-3}$)
D_k	mass diffusivity of species, k ($m^2\ s^{-1}$)
EW	equivalent weight of dry membrane ($kg\ mol^{-1}$)
F	Faraday constant (96,487 $C\ mol^{-1}$)
i_0	exchange current density ($A\ m^{-2}$)
j	transfer current density ($A\ m^{-3}$)
j^i	diffusive mass flux of ith phase ($kg\ m^{-2}\ s^{-1}$)
J	Leverett function
h	enthalpy per unit mass ($kJ\ kg^{-1}$)
k	thermal conductivity ($W\ m\ K^{-1}$)
k_r	relative permeability
K	hydraulic permeability (m^2)
M	molecular weight ($kg\ mol^{-1}$)
m	mass fraction (a scalar with no units)
n	number of electrons in electrochemical reaction or diffusivity correction factor
n_c	catalyst coverage coefficient
n_d	electro-osmotic drag coefficient
P	pressure (Pa)
P_c	capillary pressure (Pa)
RH	relative humidification of inlet
R_u	universal gas constant ($8.314\ J\ mol^{-1}\ K^{-1}$)
s	stoichiometric coefficient in electrochemical reaction or liquid saturation
S	source term in transport equation
t	time (s)
T	temperature (K)
$\boldsymbol{u}$	fluid velocity and superficial velocity in porous medium ($m\ s^{-1}$)
U_o	thermodynamic equilibrium potential (V)
V	volume (m^3)
V_{cell}	cell potential (V)

Greeks letters

α	transfer coefficient
δ_i	thickness of component i
ε	volume fraction of gaseous phase in porous region
ε_e	volume fraction of ionomer phase in CL
γ	advection correction factor
λ	membrane water content ($mol\ H_2O/mol\ SO_3^-$)
λ^α	relative mobility of phase, α
ϕ	phase potential (V)
η	overpotential (V)
θ	contact angle (°)
μ	viscosity ($kg\ m^{-1}\ s^{-1}$)
ρ	density ($kg\ m^{-3}$)
ρ^{mem}	dry membrane density ($kg\ m^{-3}$)
υ	kinematic viscosity ($m^2\ s^{-1}$)
σ	surface tension ($N\ m^{-1}$) or electronic conductivity ($S\ m^{-1}$)
τ	viscous shear stress ($N\ m^{-2}$)
κ	ionic conductivity ($S\ m^{-1}$)
ξ	stoichiometric flow ratio

Superscripts

c	cathode or capillary
e	electrolyte
eff	effective value in porous region
mem	membrane
g	gas
l	liquid
ref	reference value
s	solid
sat	saturation value

Subscripts

a	anode
avg	average value
BP	bipolar plate
c	cathode or capillary
CL	catalyst layer
e	electrolyte
g	gas phase
GC	gas channel
GDL	gas diffusion layer
H_2	hydrogen
i	species index
in	channel inlet
m	mass equation
mem	membrane
N_2	nitrogen
O_2	oxygen
ref	reference value
t	total
s	solid
sat	saturation value
w	water
Φ	potential equation
0	standard condition, 298.15 K and 101.3 kPa (1 atm)

performance than the latter. They hypothesized that the beneficial effect of dry-layer MPLs is due to a relatively larger number of meso-pores that remain open for gas transport for PEFC operations under conditions of high humidification. Ong et al. [12] examined the effect of MPLs, which were based on PVDF (polyvinylidene fluoride), as a function of several material-dependent parameters, such as the PVDF concentration, PVDF/electrically conductive filler ratio, and MPL thickness. Ramasamy et al. [13] emphasized the influence of MPLs on PEFC durability. By measuring the water-retention capacities of new and aged GDL samples, it was found that GDL samples continuously lose their hydrophobicity during long-term PEFC operations and that the presence of an MPL mitigates the loss of hydrophobicity. Atiyeh et al. [14] experimentally investigated the effect of MPLs on water transport and PEFC performance. The data indicated that the presence of an MPL on the cathode side induces better overall PEFC performance but does not enhance back-diffusion of water from the cathode to the anode. Therefore, it was concluded that the advantage of using an MPL in PEFCs is associated neither with an enhanced back-diffusion of water nor with a lowered net water drag coefficient through the membrane (this coefficient is the moles of water dragged from the anode through the membrane to the cathode per mole of protons transported). By contrast, with direct methanol fuel cells (DMFCs), Liu and Wang [15] demonstrated that the use of an MPL has a dramatic effect on the net water drag coefficient through the membrane.

On the other hand, the role of MPLs in overall water transport in PEFCs was precisely investigated from a theoretical perspective [16–19]. Several MPL models have been introduced. Nam and Kaviany [16] developed a one-dimensional (1D) fuel-cell model in which an MPL was included between the cathode CL and the GDL. Based on capillary water-transport theory, it was demonstrated that the water transport through a porous medium can be enhanced by

the spatial variation of several pore-structure parameters (pore size, hydrophobicity, etc.). The 1D simulation results predicted a discontinuity in the liquid saturation profiles at the interface between the fine (MPL) and coarse (GDL) porous layers. It was concluded that the use of MPLs reduces the accumulation of liquid water in the GDL and MPL, thereby facilitating water removal from the cathode CL to the GDL. Pasaogullari and Wang [17] introduced a 1D two-phase PEFC model based on the multiphase mixture (M^2) model previously developed by Wang and Cheng [20]. Based on their 1D simulation results, they concluded that the presence of a discontinuity of liquid saturation at the interface between an MPL and a GDL enhances the removal of liquid water through the cathode GDL and consequently, reduces the liquid saturation level in the cathode CL. It should be noted that both the early MPL models developed by Nam and Kaviany [16] and Pasaogullari and Wang [17] were based on half-cell models and therefore were, unable to capture water-transport phenomena across the membrane. Subsequently, Pasaogullari and Wang [18] and Weber and Newman [19] developed 1D full-cell models that accounted for both anode and cathode GDLs and the membrane. The studies indicated that when an MPL is employed between the cathode CL and the GDL, the water back-flow across the membrane toward the anode is enhanced by buildup of hydraulic pressure in the cathode CL because a much higher capillary pressure is required to penetrate through the cathode MPL. It is reported that the enhanced water transport across the membrane helps to prevent membrane dehydration as well as serious flooding in the cathode GDL.

Although significant efforts have been targeted at clarifying the role of MPLs on overall water transport and performance, the detailed function of an MPL in increasing PEFC performance and durability is still under debate and remains unclear. This can be ascribed to a lack of experimental data that clearly represent the effects of MPLs on water transport in PEFCs. Furthermore, the MPL models developed earlier [16–19] were all based on simplified, 1D, isothermal fuel-cell models in which several key effects were missed, particularly for a non-isothermal two-phase situation. While isothermal two-phase modeling can be performed in 1D, i.e., in the through-plane direction, as commonly done in the literature [16–19], non-isothermal two-phase modeling should be multi-dimensional, due to two important additional phenomena, namely, vapor-phase diffusion driven by the thermal gradient in the two-phase region and the heat pipe effect due to transfer of latent heat from evaporation in the catalyst layer (hot region) and recondensation over the land (cold region). Both phenomena mainly depend on the in-plane thermal gradient between the channel and the land, which indicates that a two-dimensional, cross-sectional geometry considering both through-plane and in-plane variations is a minimum platform to study non-isothermal, liquid water transport in GDL/MPL. This study presents a fully three-dimensional (3D), multi-phase, fuel-cell model that couples electrochemical and thermal phenomena. In addition, numerical MPL model to assess the effects of MPLs on water transport and flooding phenomena is developed and incorporated with the fuel-cell model. The objective of this work is threefold:

(1) to present a numerical MPL model that can be incorporated with existing, multi-dimensional, fuel-cell CFD (computational fluid dynamics) models and can enable a comprehensive numerical study of MPLs;
(2) to investigate the effects of an MPL on water and temperature distributions inside PEFCs by performing numerical fuel-cell simulations;
(3) to clarify the role of an MPL in improving PEFC performance and provide a fundamental explanation of MPL functions.

The paper is laid out as follows. It starts with a brief summary of a multi-dimensional, two-phase, fuel-cell model that was developed earlier [21–23], along with a detailed description and derivation of the numerical MPL model. Numerical simulations are carried out and the role of an MPL is examined in detail under various operating conditions of PEFCs and properties of GDLs and MPLs. Finally, major conclusions are drawn, that clearly elucidate the benefits of an MPL with regard to water management and PEFC performance.

2. Numerical model

2.1. Multi-dimensional fuel-cell model

The two-phase, non-isothermal PEFC model used in the numerical MPL study was based on the multiphase mixture (M^2) model developed by Wang and Cheng [20]. Tables 1–4 briefly summarize the governing equations of the fuel-cell model, relevant source terms, electrochemical correlations, and transport properties in the electrolyte phase, respectively. Other details related to the PEFC model are available in [21–23].

2.1.1. Assumptions of model

Employing the M^2 formulation to describe two-phase transport in PEFCs, the present two-phase PEFC model makes the following assumptions:

(1) ideal gas mixtures in a single-phase region;
(2) laminar flow due to small flow velocities;
(3) isotropic porous media (GDLs, MPLs, CLs);
(4) two-phase mist flow (i.e., homogeneous flow) in GCs, assuming that channel flooding is minimal where tiny droplets exist and travel with the gas velocity inside the GCs.

2.1.2. Properties of two-phase transport

The two-phase mixture properties are defined as a function of s and $(1-s)$, which denote the volume fractions of the open pore

Table 1
Two-phase steady-state PEFC model: governing equations.

	Governing equations	
Mass	$\nabla\cdot(\rho\vec{u}) = S_m$	(1)
Momentum	Flow channels (Navier–Stokes equations): $(1/\varepsilon^2)\nabla\cdot(\rho\vec{u}\vec{u}) = -\nabla p + \nabla\cdot\tau$	(2)
	Porous media (Darcy's equations): $\rho\vec{u} = -(K/\nu)\nabla p$	(3)
Species	Flow channels and porous media: $\nabla\cdot(\gamma_i\rho m_i\vec{u}) = \nabla\cdot[\rho^g D_i^{g,eff}\nabla(m_i^g)] + \nabla\cdot[(m_i^g - m_i^l)\vec{j}^l] + S_i$	(4)
	Water transport in membrane: $\nabla\cdot((\rho^{mem}/EW)D_w^{mem}\nabla\lambda)M_w - \nabla\cdot(n_d(I/F))M_w + \nabla\cdot((K^{mem}/\nu^l)/\nabla P^l) = 0$	(5)
Charge	Proton transport: $\nabla\cdot(\kappa^{eff}\nabla\Phi_e) + S_\Phi = 0$	(6)
	Electron transport: $\nabla\cdot(\sigma^{eff}\nabla\Phi_s) - S_\Phi = 0$	(7)
Energy	$\nabla\cdot(\rho\vec{u}C_p^g T) = \nabla\cdot(k^{eff}\nabla T) + \nabla\cdot(h_{fg}^o\rho^l\vec{u}^l) + S_T$	(8)

Table 2
Two-phase steady-state PEFC model: source/sink terms.

	Source/sink terms	
Mass	In the CLs: $S_m = \sum_i S_i + M_w \nabla \cdot (D_w^{mem}(\rho^{mem}/EW)\nabla\lambda)$	(9)
Species	For water in CLs: $S_i = M_i[-\nabla \cdot ((n_d/F)I) - (s_i j/nF)]$	(10)
	For other species in CLs: $S_i = -M_i(s_i j/nF)$	(11)
Charge	In CLs: $S_\Phi = j$	(12)
Energy	In CLs: $S_T = j(\eta + T(dU_o/dT)) + (I^2/\kappa^{eff})$	(13)
	In membrane: $S_T = I^2/\kappa^{eff}$	(14)

spaces that are occupied by the liquid and gas phases, respectively [20].

Density [20]:

$$\rho = \rho^l \cdot s + \rho^g \cdot (1 - s). \tag{24}$$

In Eq. (24), the gas mixture density, ρ^g, as described by the ideal gas law, varies with the composition of the mixture (denoted here by the mass fractions, $\{m_i^g\}$). That is

$$\rho^g = \left(\frac{P}{R_u T}\right) \frac{1}{\sum_i m_i^g / M_i}. \tag{25}$$

Velocity [20]:

$$\rho\vec{u} = \rho^l \vec{u}^l + \rho^g \vec{u}^g. \tag{26}$$

Relative permeability:

$$k_r^l = s^4 \tag{27}$$

and

$$k_r^g = (1 - s)^4. \tag{28}$$

Kinematic viscosity [20]:

$$\upsilon = \left(\frac{k_r^l}{\nu^l} + \frac{k_r^g}{\nu^g}\right)^{-1}. \tag{29}$$

In Eq. (29), ν^g is the kinematic viscosity of the gas mixture that varies with the gas composition [24]:

$$\upsilon^g = \frac{\mu^g}{\rho^g} = \frac{1}{\rho^g} \sum_{i=1}^{n} \frac{x_i \mu_i}{\sum_{j=1}^{n} x_j \Phi_{ij}}, \quad \text{where}$$

$$\Phi_{ij} = \frac{1}{\sqrt{8}} \left(1 + \frac{M_i}{M_j}\right)^{-1/2} \left[1 + \left(\frac{\mu_i}{\mu_j}\right)^{1/2} \left(\frac{M_j}{M_i}\right)^{1/4}\right] \tag{30}$$

and

$$\mu_i\,[\mathrm{N\,s\,m^{-2}}] = \begin{cases} \mu_{H_2} = 0.21 \times 10^{-6} T^{0.66} \\ \mu_w = 0.00584 \times 10^{-6} T^{1.29} \\ \mu_{N_2} = 0.237 \times 10^{-6} T^{0.76} \\ \mu_{O_2} = 0.246 \times 10^{-6} T^{0.78} \end{cases}, \quad T \text{ in Kelvin.}$$

Relative mobility [20]:

$$\lambda^l = \frac{k_r^l}{\nu^l} \nu, \tag{31}$$

$$\lambda^g = 1 - \lambda^l. \tag{32}$$

Table 3
Electrochemical correlations.

Electrochemical reactions: $\sum_k s_i M_i^z = ne^-$, where $\begin{cases} M_i \equiv \text{chemical formula of species } i \\ s_i \equiv \text{stoichiometry coefficient} \\ n \equiv \text{number of electrons transferred} \end{cases}$	(15)
Hydrogen oxidation reaction (HOR) in anode side: $H_2 - 2H^+ = 2e^-$	(16)
Transfer current density [$\mathrm{A\,m^{-3}}$]: $j = (1-s)^{n_c} a i_{0,a}^{ref} \left(\frac{C_{H_2}}{C_{H_2,ref}}\right)^{1/2} \left(\frac{\alpha_a + \alpha_c}{R_u T} F\eta\right)$	(17)
Surface overpotential [V]: $\eta = \phi_s - \phi_e$	(18)
Oxygen reduction reaction (ORR) in cathode side: $2H_2O - O_2 - 4H^+ = 4e^-$	(19)
Transper current density [$\mathrm{A\,m^{-3}}$]: $j = -(1-s)^{n_c} a i_{0,c}^{ref} \left(\frac{C_{O_2}}{C_{O_2,ref}}\right)^{3/4} \exp\left(-\frac{\alpha_c}{R_u T} F\eta\right)$	(20)
Surface overpotential [V]: $\eta = \phi_s - \phi_e - U_o$	(21)
Thermodynamic equilibrium potential: $U_o = 1.23 - 0.9 \times 10^{-3}(T - 298.15)$	(22)
Temperature dependence of ORR kinetic parameter: $a i_{0,c}^{ref}(T) = a i_{0,c}^{ref}(353K) \exp\left[-\frac{E_a}{R_u}\left(\frac{1}{T} - \frac{1}{353.15}\right)\right]$	(23)

Table 4
Transport properties in electrolyte phase.

Expression	Ref.
Water activity: $a = \frac{C_w^g R_u T}{P_{sat}}$	[26]
Water content: $\lambda = \begin{cases} \lambda^g = 0.043 + 17.81a - 39.85a^2 + 36.0a^3 & \text{for } 0 < a \le 1 \\ \lambda^l = 22 \end{cases}$	[26]
Electro-osmotic drag coefficient: $n_d = \frac{2.5\lambda}{22}$	[26]
Water diffusion coefficient in membrane: $D_w^{mem} = \begin{cases} 2.692661843 \times 10^{-10} & \text{for } \lambda \le 2 \\ \{0.87(3-\lambda) + 2.95(\lambda - 2)\} \times 10^{-10}\, e^{(7.9728 - (2416/T))} & \text{for } 2 < \lambda \le 3 \\ \{2.95(4-\lambda) + 1.642454(\lambda - 3)\} \times 10^{-10}\, e^{(7.9728 - (2416/T))} & \text{for } 3 < \lambda \le 4 \\ (2.563 - 0.33\lambda + 0.0264\lambda^2 - 0.000671\lambda^3) \times 10^{-10}\, e^{(7.9728 - (2416/T))} & \text{for } 4 < \lambda \le \lambda_{a=1}^g \end{cases}$	[26]
Proton conductivity: $\kappa = (0.5139\lambda - 0.326) \exp\left[1268\left(\frac{1}{303} - \frac{1}{T}\right)\right]$	[26]

The effective diffusivity of species i in the gas mixture:

$$D_i^{g,eff} = [\varepsilon(1-s)]^n \left(\frac{1}{D_i^g} + \frac{1}{D_i^K}\right)^{-1}, \tag{33}$$

where D_i^g and D_i^K respectively denote the species diffusivity in the gas mixture and the Knudsen diffusion coefficient, which are expressed as follows.

Species diffusivity in the gas mixture [24]:

$$D_i^g = \frac{1-x_i}{\sum_{\substack{j=n \\ j\neq i}} x_j/D_{i,j}}, \quad \text{where}$$

$$D_{i,j} = \frac{1.013\times10^{-7}\cdot T^{1.75}}{p\cdot(\chi_i^{1/3}+\chi_j^{1/3})^2}\cdot\left(\frac{1}{M_i}+\frac{1}{M_j}\right)^{1/2},$$

$$\chi_{H_w} = 7.07,\quad \chi_w = 12.7,\quad \chi_{N_w} = 17.9,\quad \chi_{O_w} = 16.6. \tag{34}$$

The Knudsen diffusion coefficient:

$$D_i^K = \frac{2}{3}\left(\frac{8R_uT}{\pi M_i}\right)^{1/2} r_p. \tag{35}$$

Diffusive mass flux of the liquid phase [20]:

$$\vec{j}^l = \rho^l\vec{u}^l - \lambda^l\rho\vec{u} = \frac{K}{\nu}\lambda^l\lambda^g\nabla P_c, \tag{36}$$

where the capillary pressure, P_c, and the Leverett function, $J(s)$ are computed as below:

$$P_c = P^g - P^l = \sigma\cos\theta\left(\frac{\varepsilon}{K}\right)^{1/2} J(s), \tag{37}$$

$$J(s) = \begin{cases} 1.417(1-s) - 2.120(1-s)^2 + 1.263(1-s)^3 & \text{if } \theta_c < 90^\circ \\ 1.417s - 2.120s^2 + 1.263s^3 & \text{if } \theta_c > 90^\circ \end{cases}. \tag{38}$$

Advection correction factor [20]:

$$\gamma_i = \frac{\rho(\lambda^l m_i^l + \lambda^g m_i^g)}{(s\rho^l m_i^l + (1-s)\rho^g m_i^g)}. \tag{39}$$

2.1.3. The numerical MPL model

The development of the numerical MPL model starts with the balance of liquid pressure across the interface between an MPL and GDL:

$$P_{MPL}^l = P_{GDL}^l. \tag{40}$$

The overall liquid pressure of an MPL or GDL in Eq. (40) is separated into two parts, namely, the pressure of liquid water transportable by capillary action, P_c^l, and the liquid-entry pressure, P_{entry}^l, which represents a threshold pressure to penetrate a given porous layer (MPL or GDL). Therefore, Eq. (40) can be expressed in terms of these two pressures as follows:

$$\begin{gathered} P_{MPL}^l = P_{c,MPL}^l + P_{entry,MPL}^l = P_{c,GDL}^l + P_{entry,GDL}^l = P_{GDL}^l \\ P_{c,MPL}^l + P_{entry}^l = P_{c,GDL}^l \end{gathered}, \tag{41}$$

where P_{entry}^l represents the relative liquid-entry pressure difference between a GDL and MPL due to the differing pore structures and wettabilities.

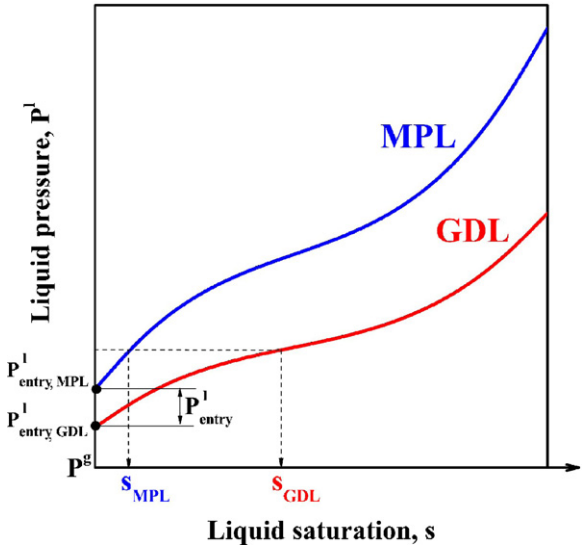

Fig. 1. Liquid pressure vs. liquid saturation curves for hydrophobic media.

Using the capillary pressure definition given by Eq. (37), the balance of liquid pressure can be written in terms of the capillary and gas pressures as follows:

$$-P_{c,MPL} + P_{MPL}^g + P_{entry}^l = -P_{c,GDL} + P_{GDL}^g. \tag{42}$$

Since the gas pressure should be continuous at the interface ($P_{MPL}^g = P_{GDL}^g$), by using Eq. (37), the final form of the liquid pressure-balance term in Eq. (40) can be expressed as two-phase transport parameters in terms of the capillary pressure:

$$\begin{gathered} -P_{c,MPL} + P_{entry}^l = -P_{c,GDL} \\ -\sigma\cos(\theta_{MPL})\left(\frac{\varepsilon_{MPL}}{K_{MPL}}\right)^{1/2} J(s_{int,MPL}) + P_{entry}^l = -\sigma\cos(\theta_{GDL})\left(\frac{\varepsilon_{GDL}}{K_{GDL}}\right)^{1/2} J(s_{int,GDL}) \end{gathered}, \tag{43}$$

where $s_{int,MPL}$ and $s_{int,GDL}$ respectively denote the liquid saturations of the MPL and GDL at the interface. Fig. 1, which is a plot of Eq. (43) that uses reasonable MPL and GDL properties, clearly illustrates a discontinuity in the liquid saturation across the GDL|MPL interface. There are two unknown variables, $s_{int,MPL}$ and $s_{int,GDL}$, in Eq. (43); this requires the solution of one more equation that can be obtained by satisfying the continuity of water flux across the interface. The water-species equation for the GDL and MPL region can be simplified by neglecting the convection term, due to the small velocity in these porous layers:

$$0 = \nabla\cdot[\rho^g D_i^{g,eff}\nabla(m_i^g)] + \nabla\cdot[(m_i^g - m_i^l)\vec{j}^l], \tag{44}$$

where the first and second terms in the right-hand-side represent the vapor-phase diffusion and capillary transport for the two-phase region. As schematically shown in Fig. 2, the water flux continuity at the interface can be written in a discretized form by combining Eqs. (37), (38) and (44) as follows:

$$\begin{gathered} m_{mpl} = m_{w,MPL} = m_{w,GDL} \\ \rho^g D_w^{g,eff})_1 \frac{m_{w,1}^g - m_{int,MPL}^g}{\Delta x_1/2} + (m_w^g - m_w^l)\frac{(\varepsilon K)^{1/2}}{\nu}\lambda^l\lambda^g\sigma\cos(\theta)\frac{dJ}{ds}\Big)_1 \frac{s_1 - s_{int,MPL}}{\Delta x_1/2} \\ = \rho^g D_w^{g,eff})_2 \frac{m_{int,GDL}^g - m_{w,2}^g}{\Delta x_2/2} + (m_w^g - m_w^l)\frac{(\varepsilon K)^{1/2}}{\nu}\lambda^l\lambda^g\sigma\cos(\theta)\frac{dJ}{ds}\Big)_2 \frac{s_{int,GDL} - s_2}{\Delta x_2/2} \end{gathered}. \tag{45}$$

Therefore, the values of the liquid saturation at the interface, viz., $s_{int,MPL}$ and $s_{int,GDL}$, can be obtained by solving Eqs. (43) and

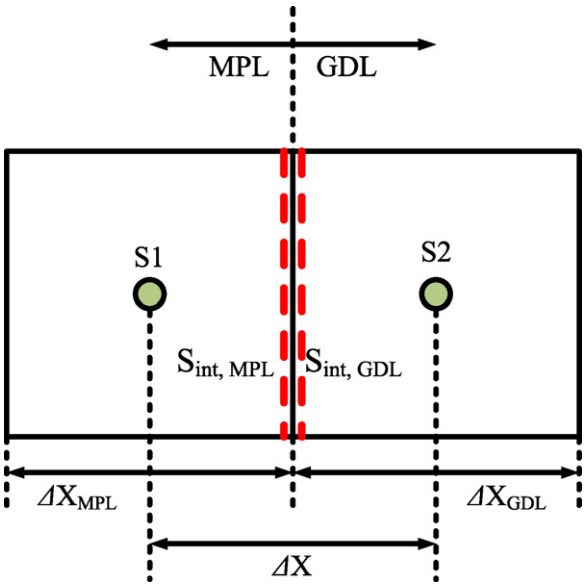

Fig. 2. Schematic of computational grid at interface between the cathode MPL and GDL for numerical implementation of MPL model to predict a discontinuity in liquid saturation.

(45). Finally, the additional water-source term for the numerical MPL model has to be applied to the water-species equation of the current two-phase fuel-cell model as follows:

$$S_{mpl} = \begin{cases} 0 & \text{for single-phase region} \\ \nabla \cdot m_{mpl} & \text{for two-phase region} \end{cases}. \quad (46)$$

2.2. Boundary conditions and numerical implementation

The inlet velocities in the anode and cathode gas channels (GCs) can be expressed as a function of the anode and cathode stoichiometric ratios (ξ_a and ξ_c, respectively), the PEFC operating current density (I), the cross-sectional areas of the anode and cathode GCs (A_a and A_c, respectively), and the densities of hydrogen gas or air, which are respectively a function of the anode/cathode inlet pressure, temperature, and humidity:

$$u_{in,a} = \frac{\xi_a (I/2F) A_{mem} M_{H_2}}{\rho_{H_2} A_a} \quad \text{and} \quad u_{in,c} = \frac{\xi_c (I/4F) A_{mem} M_{O_2}}{\rho_{O_2} A_c}. \quad (47)$$

In addition, an isothermal boundary condition (80 °C for this study) is applied to the outer surfaces of the bipolar plate for temperature calculations. The two-phase PEFC model coupled with the numerical MPL model described above is numerically implemented with a commercially available, computational fluid dynamics (CFD) package, namely, STAR-CD, through its user-subroutine files [25].

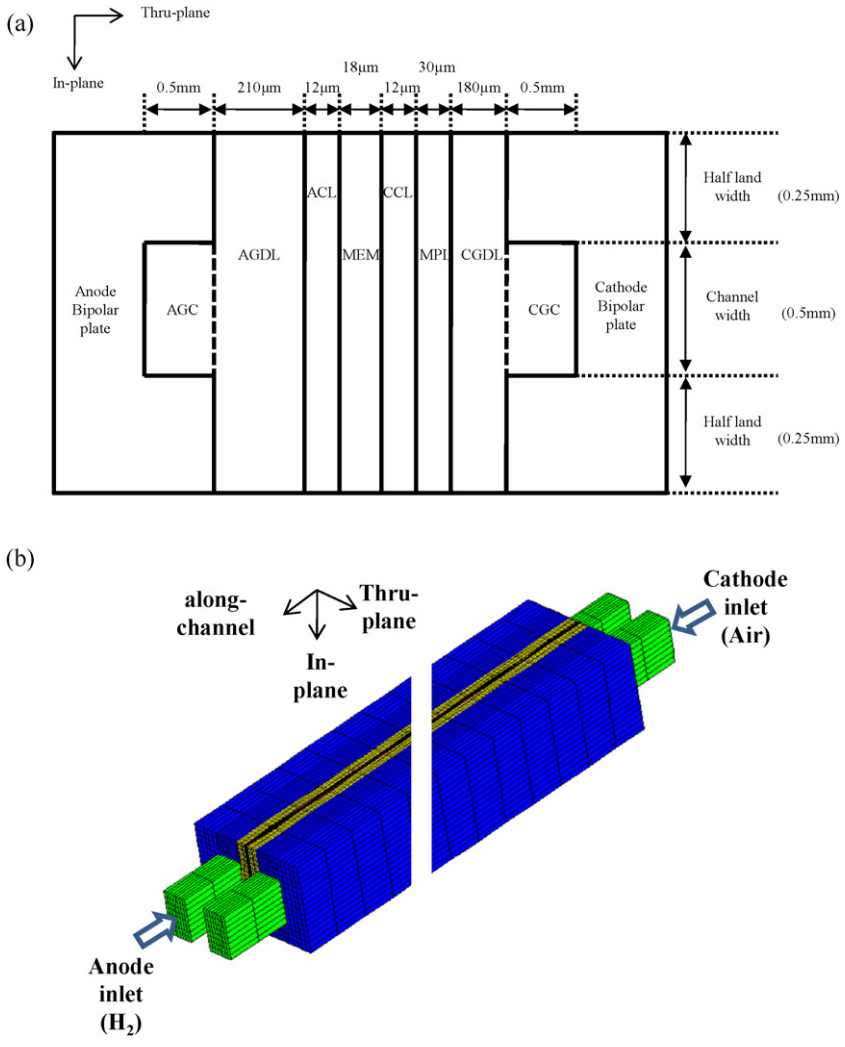

Fig. 3. Three-dimensional, single-channel, PEFC geometry: (a) dimensions and (b) mesh configuration.

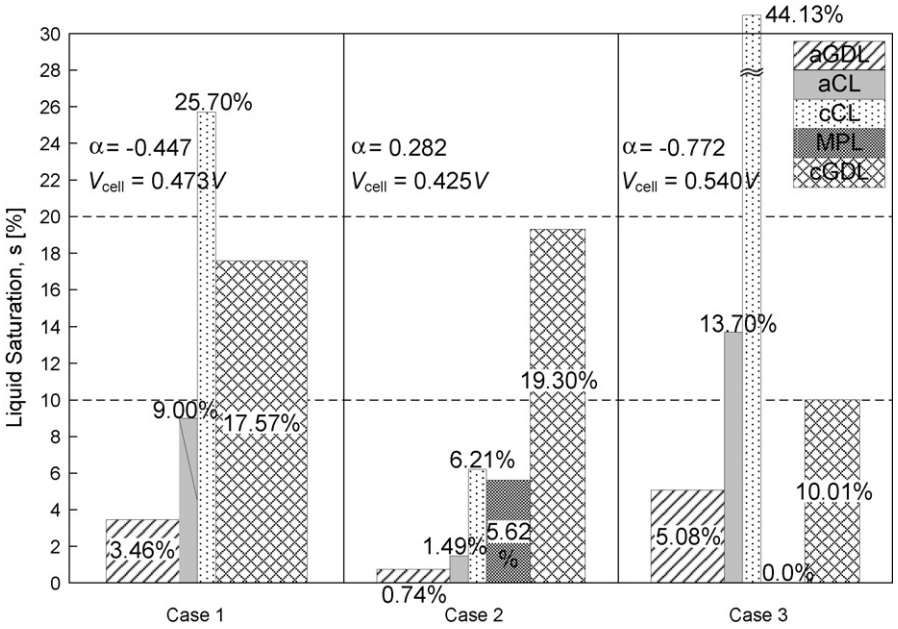

Fig. 4. Comparison of simulation results in terms of: average liquid saturation (s) accumulated in PEFC components; net water-transport coefficient (α) through membrane; and cell performance (V_{cell}) at 1.5 A cm^{-2}.

3. Results and discussion

In this study, a comprehensive two-phase, non-isothermal, PEFC model is applied to a typical fuel-cell geometry with an MPL at the cathode side, as schematically shown in Fig. 3(a); the mesh configuration is displayed in Fig. 3(b). It is seen in Fig. 3 that PEFC operation is based on the counter-flow configuration of hydrogen in the anode GC and air in the cathode GC. The properties of the individual cell components and the operating conditions are listed in Table 5 and the physical properties are summarized in Table 6. It should be noted that the two-phase transport properties of the catalyst layer are assumed to be same as those of MPL to facilitate the present MPL analysis for two-phase transport phenomena between an MPL and a GDL.

To analyze the role of an MPL in PEFC operation, three cases have been defined for this study. Case 1 eliminates the effect of an MPL at the cathode side by applying the properties of a GDL in Table 5 to the MPL, while the true MPL properties in Table 5 are employed for cases 2 and 3. The contrast between cases 2 and 3 is related to the relative liquid-entry pressure difference between the GDL and the MPL, which is seen in Eq. (40). Case 2 considers the difference in porous properties between the GDL and the MPL but neglects the effect of the liquid-entry pressure difference, even though a much higher liquid-entry pressure is expected in an MPL than in a GDL due to the finer pore structure of the former. Therefore, it is expected in case 2 that a saturation jump occurs at the GDL|MPL interface because the capillary pressure is continuous across the interface, which means that the liquid water saturation in the MPL is much smaller than that in the GDL because of the smaller pore size and greater hydrophobicity in the MPL. On the other hand, case 3 additionally considers a high liquid-entry pressure in an MPL, i.e., 100 kPa. Since the pore sizes of an MPL are usually smaller than 1 μm, it is reasonable to assume a high value of the liquid-entry pressure of the MPL. Consequently, it is expected that in case 3, the capillary-driven liquid water pressure in the GDL is far below the liquid-entry pressure of the MPL, which prevents any liquid water from entering the MPL. These three cases have been simulated at two current densities, namely, 0.5 and 1.5 A cm^{-2}; so, altogether, six simulations are carried out in this study.

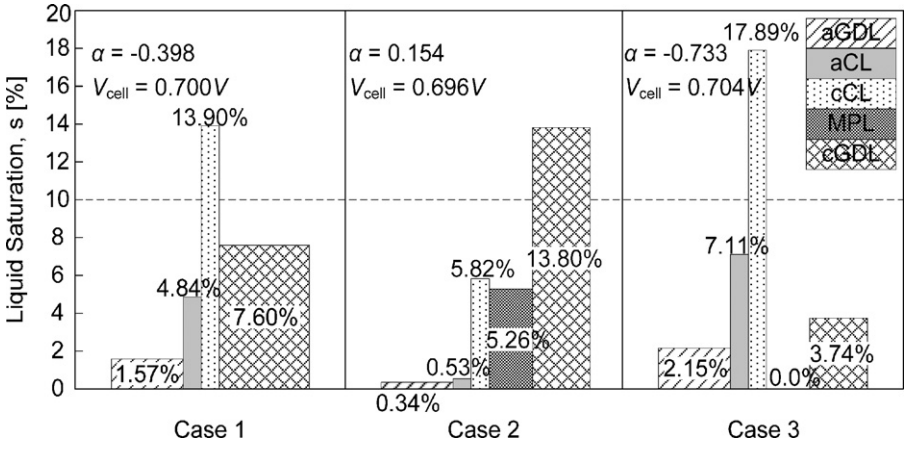

Fig. 5. Comparison of simulation results in terms of: average liquid saturation (s) accumulated in PEFC components; net water-transport coefficient (α) through membrane; and cell performance (V_{cell}) at 0.5 A cm^{-2}.

Table 5
Cell properties and operating conditions.

Description	Value
Porosity of GDL (ε_{GDL})	0.7
Porosity of MPL (ε_{MPL})	0.6
Porosity of CL (ε_{CL})	0.6
Volume fraction of ionomer in CLs (ε_{mc})	0.23
Permeability of GDL (K_{GDL})	1.0×10^{-12} m^2
Permeability of MPL (K_{MPL})	1.0×10^{-13} m^2
Permeability of CL (K_{CL})	1.0×10^{-13} m^2
Hydraulic permeability of membrane (K_{mem})	5.0×10^{-20} m^2
Contact angle of GDL (θ_{GDL})	110°
Contact angle of MPL (θ_{MPL})	120°
Contact angle of CL (θ_{CL})	120°
Effective electronic conductivity in GDL (σ_{GDL})	10,000 S m^{-1}
Effective electronic conductivity in MPL (σ_{MPL})	1000 S m^{-1}
Effective electronic conductivity in CL (σ_{CL})	1000 S m^{-1}
Effective electronic conductivity in BP (σ_{BP})	20,000 S m^{-1}
Thermal conductivity of GDL (k_{GDL})	5.0 W m^{-1} K^{-1}
Thermal conductivity of MPL (k_{MPL})	1.0 W m^{-1} K^{-1}
Thermal conductivity of CL (k_{CL})	1.0 W m^{-1} K^{-1}
Thermal conductivity of BP (k_{BP})	20.0 W m^{-1} K^{-1}
Thermal conductivity of membrane (k_{mem})	0.95 W m^{-1} K^{-1}
Anode/cathode inlet pressure (P_a/P_c)	1.5 atm/1.5 atm
Anode/cathode stoichiometry (ξ_a/ξ_c)	2/2
Anode/cathode inlet relative humidity at 353.15 (RH_a/RH_c)	100%/100%

For cases 1–3 at 1.5 A cm^{-2}, Fig. 4 shows the variation of the amount of the average liquid water that is accumulated in an individual PEFC component along the through-plane direction with (a) the cell performance and (b) the net water-transport coefficient through the membrane. The net water-transport coefficient that is denoted by "α" implies that the net water flux across the membrane is normalized by the protonic flux as follows:

$$\alpha = \frac{n_d(I/F) - ((\rho^{mem}/EW)D_w^{mem}\nabla\lambda + (K^{mem}/\nu^l)\nabla P^l)}{I/F}. \quad (48)$$

First, for case 1 (no MPL effect), the amount of liquid water continuously decreases from the inside of the cell, i.e., CL, toward the outside, i.e., GC, and no discontinuity is observed in the liquid saturation. On the other hand, it is seen for case 2 (MPL without the liquid-entry pressure effect) that a discontinuity in the liquid saturation across the cathode MPL|GDL interface exists due to differences in the porous properties and wetting characteristics between the MPL and the GDL. The average liquid saturation in the MPL is lower than that in the cathode GDL due to the relatively higher hydrophobicity and smaller pore size of the MPL. Therefore, the MPL in case 2 helps to lower the amount of liquid water in the cathode CL that, in turn, significantly reduces the back-flow of water across the membrane from the cathode to the anode, thereby rendering the net water-transport coefficient, α, of case 2 positive and the highest among cases 1–3. Consequently, a larger portion of excessive product water in the cathode CL is transported toward the cathode side, raising the amount of liquid water in the cathode GDL.

For case 3 (MPL with the liquid-entry pressure effect), the MPL is free of liquid water (zero liquid saturation) due to its high liquid-

Table 6
Physical properties.

Description	Value
Exchange current density × Ratio of reaction surface to CL volume in anode side ($ai_{0,a}^{ref}$)	1.0×10^9 A m^{-3}
Exchange current density × Ratio of reaction surface to CL volume in cathode side ($ai_{0,c}^{ref}$)	2.0×10^4 A m^{-3}
Activation energy for the oxygen reduction reaction in cathode side (E_a)	73,269 J mol^{-1}
Reference hydrogen molar concentration ($c_{H_2,ref}$)	40.88 mol m^{-3}
Reference oxygen molar concentration ($c_{O_2,ref}$)	40.88 mol m^{-3}
Anodic and cathodic transfer coefficients for hydrogen oxidation reaction (HOR)	$\alpha_a = \alpha_c = 1$
Cathodic transfer coefficient for oxygen reduction reaction (ORR)	$\alpha_c = 1$
Dry membrane density (ρ^{mem})	2000 kg m^{-3}
Equivalent weight of electrolyte in membrane (EW)	1.1 kg mol^{-1}
Faraday constant (F)	96,487 C mol^{-1}
Universal gas constant (R_u)	8.314 J mol^{-1} K^{-1}
Surface tension (σ)	0.0625 N m^{-1}
Liquid water density (ρ^l (80 °C))	972 kg m^{-3}
Liquid water viscosity (μ^l)	3.5×10^{-4} N s m^{-2}

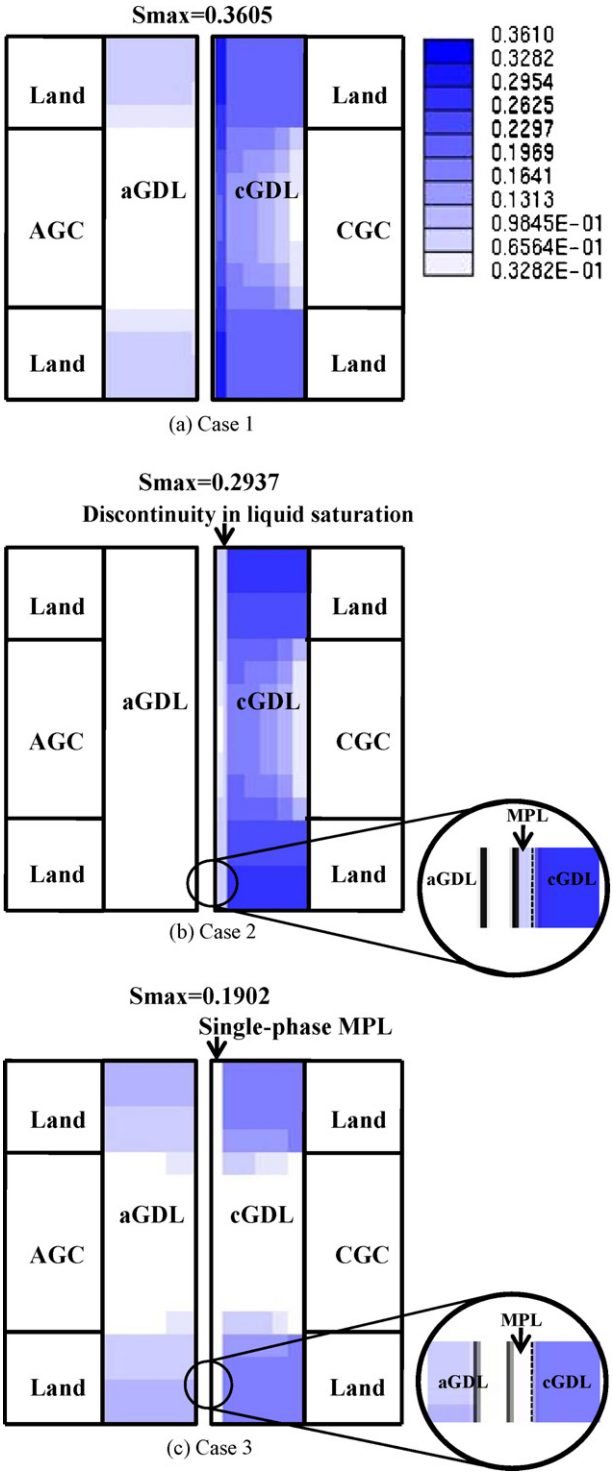

Fig. 6. (a–c) Comparison of liquid saturation contours in cross-section of anode GDL and cathode MPL/GDL at fractional distance of 0.5 from cathode inlet: $I = 1.5$ A cm^{-2}.

entry pressure, where liquid water fails to invade the MPL by capillary action and thus, only water vapor exists. This indicates that the MPL for case 3 acts as a capillary barrier, as a result of which water transport through the MPL is only driven by vapor-phase diffusion under the temperature gradient. Consequently, in case 3, the buildup of liquid water in the cathode CL, viz., 44% liquid saturation, is much higher than in cases 1 and 2 (25.7% for case 1 and 4.21% for case 2), which in turn significantly enhances the water back-flow across the membrane into the anode for this case. As a result, for case 3, α is negative and the lowest among cases 1–3. A comparison of the liquid water accumulation and α value in Fig. 4 indicates that the amount of liquid water in the anode side and α are the highest in case 3 and the lowest in case 2.

It is also seen in Fig. 4 that the differences in liquid water profiles that are predicted in cases 1–3 strongly influences cell performance. Case 3 has the highest cell performance of V_{cell} = 0.54 V at 1.5 A cm^{-2}, which is about 67 mV higher than that of case 1 and 115 mV higher than that of case 2. The higher performance in case 3 must be due to the greater back-flow of water across the membrane toward the anode in case 3, which prevents dehydration of the anode side of the membrane as well as lowers the level of GDL flooding. Therefore, the comparison of cases 1–3 in Fig. 4 clearly demonstrates that the MPL improves cell performance through improved water management that is achieved by enhancing the back-flow of water across the membrane into the anode. In addition, it is also found that the saturation jump itself at the interface of the MPL and the GDL does not help to improve PEFC performance, which conflicts with the conclusions obtained from the previously published, 1D, half-cell model simulations [16,17].

Fig. 5 presents a comparison of the average liquid water accumulations in the PEFC components at 0.5 A cm^{-2}. Although the same trend is observed as in Fig. 4, the differences in the cell performance and liquid water accumulation between cases 1–3 become smaller, which agrees with the experimental observations where the benefits of MPLs are more noticeable with operation at higher current densities. This indicates that the use of MPLs helps to decrease the ohmic and mass-transfer resistances inside a cell.

Fig. 6 displays the liquid saturation contours in the anode GDL and cathode MPL/GDL for cases 1–3 at 1.5 A cm^{-2}. No discontinuity is observed in the liquid saturation profile for case 1 (Fig. 6(a)) because the MPL is not employed in this case. On the other hand, when an MPL features between the cathode CL and GDL but the relative entry-pressure effect is ignored (case 2), the liquid saturation profile, as seen in Fig. 6(b), clearly shows that the presented numerical MPL model successfully captures a discontinuity in the liquid saturation contour at the GDL|MPL interface. This discontinuity arises from the differences in the porous properties and wettability between the MPL and the GDL. As the liquid-entry pressure effect is further considered for the MPL (case 3), it is seen from Fig. 6(c) that the single-phase MPL situation, i.e., zero liquid saturation in the MPL, is successfully predicted by the current numerical MPL model. Since the only means for water transport in the single-phase MPL is vapor-phase diffusion that is driven by the temperature gradient, a significant enhancement of water back-flow across the membrane into the anode is expected in case 3. Consequently, a comparison of the liquid water saturation contours in cases 1–3 clearly shows that the amount of liquid water in the anode side is highest in case 3.

Fig. 7 shows the water content contours at 1.5 A cm^{-2} on a CCM that includes the anode/cathode CLs and the membrane. As shown by the expressions given in Table 4, the proton conductivity, κ, increases with the water content, λ, in the electrolyte phase of the CCM and thus, a lower content of water is indicative of a greater ohmic loss in PEFCs. First, all three cases in Fig. 7 reveal that the effect of membrane dehydration is more severe near the anode side of the CCM that faces the channel region, which suggests a relatively lower value of water content there. That is because the anode CCM near the channel is prone to lose more water toward the cathode. More importantly, a comparison of the water content profiles of cases 1–3 clearly answers why the highest cell performance is achieved in case 3. The presence of an MPL with the liquid-entry pressure effect (case 3) considerably prevents dry out of the anode CCM by enhancing the back-flow of water across the membrane into the anode and as a result, the water content in the anode side

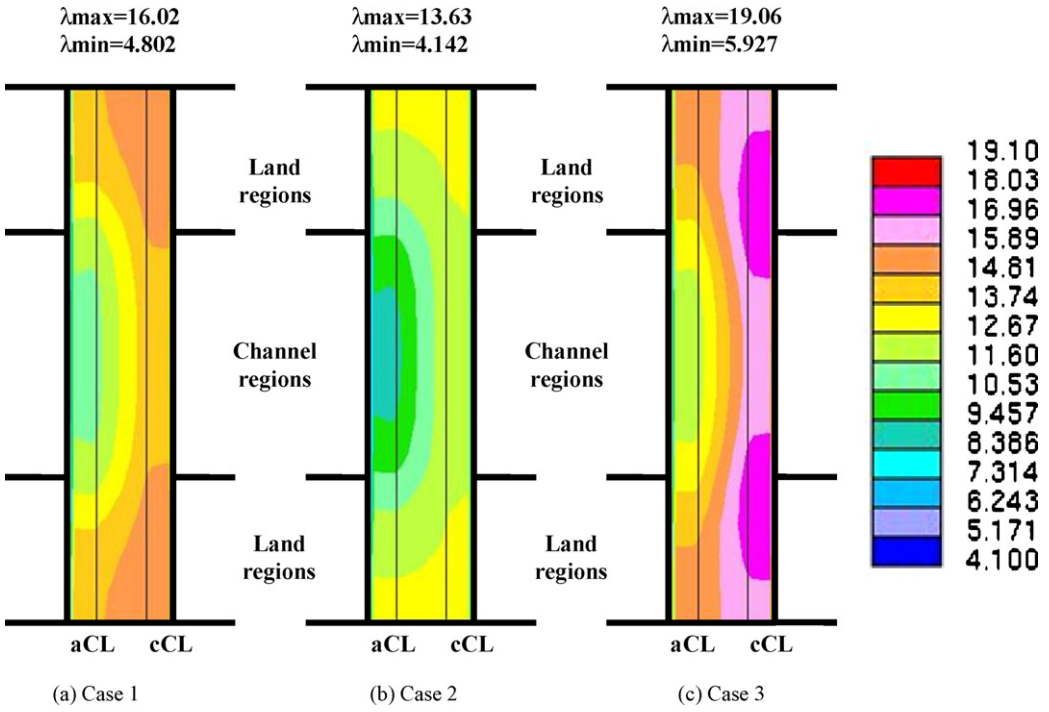

Fig. 7. (a–c) Comparison of water-content contours in cross-section of anode/cathode CLs and the membrane at fractional distance of 0.5 from cathode inlet: I = 1.5 A cm^{-2}.

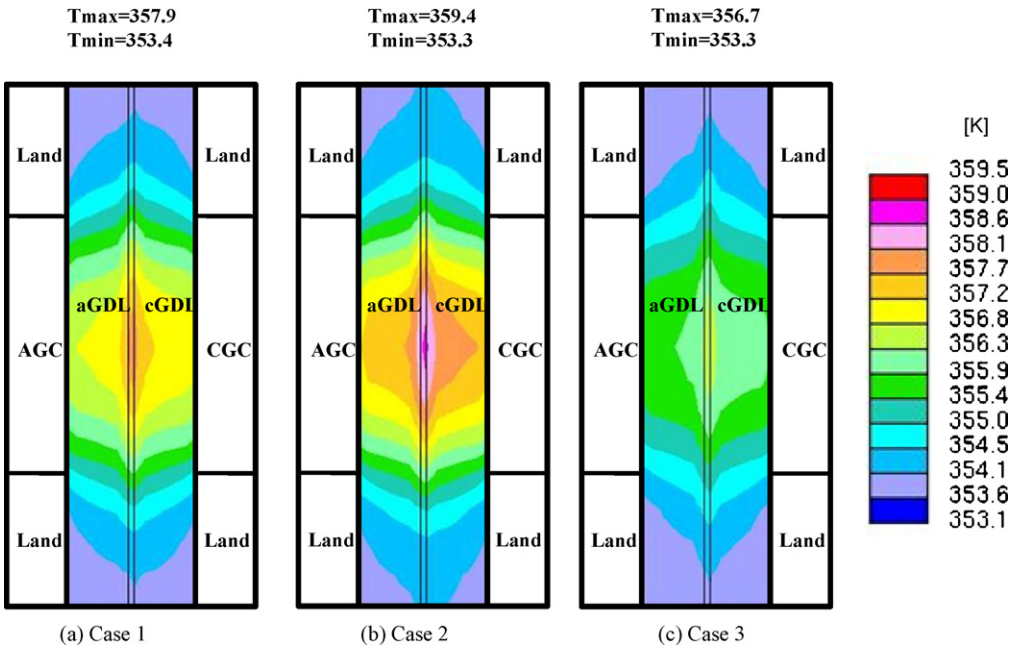

Fig. 8. (a–c) Comparison of temperature contours in cross-section of membrane electrode assembly (MEA) that includes anode/cathode GDLs, anode/cathode CLs, MPL, and membrane, at a fractional distance of 0.5 from cathode inlet: $I = 1.5\ \mathrm{A\,cm^{-2}}$.

of the CCM for case 3 is much higher than that for case 1. On the other hand, it is seen from a comparison between Fig. 7(a) and (b) that the effect of anode dry out is over-predicted in case 2 due to the under-prediction of the water flux across the membrane into the anode. The water content profiles in Fig. 7 verify the accuracy of the present numerical MPL model and clearly demonstrate the beneficial effects of an MPL on water management and the performance of PEFCs.

Fig. 8 presents the temperature contours on the anode and cathode porous layers (GDL and MPL) for cases 1–3 at $1.5\ \mathrm{A\,cm^{-2}}$. As discussed in regard to Fig. 4, the cell performance of case 3 is higher than those of cases 1 and 2 due to the effect of the single-phase MPL in case 3. As a result, the maximum rise in the temperature for case 3 (3.0 °C) is lower than those of cases 1 and 2 (4.75 °C for case 1 and 5.55 °C for case 2). Therefore, it can be emphasized that the presence of an MPL considerably affects the overall cell performance as well as the maximum temperature rise and liquid saturation profile inside a cell.

4. Conclusions

A numerical MPL model has been developed and incorporated into a comprehensive, non-isothermal, two-phase PEFC model that was published earlier [21–23]. Three-dimensional, two-phase, non-isothermal simulations have been performed to investigate precisely the role of an MPL in the distribution of temperature and water as well as cell performance. The following conclusions can be drawn.

(1) When the effect of an MPL due to differences in porous properties is taken into account but the effect of a high liquid-entry pressure is ignored (case 2), the numerical MPL model accurately capture a discontinuity in the liquid saturation at the MPL|GDL interface. The discontinuity causes a decrease in the amount of liquid water at the cathode CL that in turn reduces the water back-flow across the membrane from the cathode to anode. Consequently, the performance predicted in that case (case 2) is even lower than in the case without the MPL (case 1) due to the drier membrane as well as the higher level of GDL flooding in case 2. The result is contradictory compared with experimental observations.

(2) When a high liquid-entry pressure (100 kPa) is further applied to the MPL, the numerical MPL model predicts a single-phase MPL situation where liquid water fails to enter the MPL due to the high liquid-entry pressure. Only water vapor is transported via vapor-phase diffusion that is driven by the temperature gradient through the MPL. The mechanism significantly increases the water back-flow across the membrane into the anode. Consequently, consideration of the liquid-entry pressure enables the MPL model to predict successfully the beneficial effect of MPLs in terms of PEFC performance, where an increase of 67 mV in the performance is achieved at $1.5\ \mathrm{A\,cm^{-2}}$. The liquid saturation profiles that are predicted by the numerical simulations further indicate that the MPL mainly improves PEFC performance by achieving a more favorable water profile inside the cell. In turn, this is realized by enhancing the water back-flow across the membrane toward the anode side, avoiding dehydration of the membrane, and alleviating the level of GDL flooding.

(3) A comparison of the numerical simulation results at 0.5 and $1.5\ \mathrm{A\,cm^{-2}}$ clearly demonstrates that the effect of MPLs is more appreciable at the higher current density, which accords with the trend observed in much experimental data. This indicates that the beneficial effect of MPLs on PEFC performance is due to reduction in both the ohmic and the mass-transfer resistance. The numerical MPL model successfully captures the MPL phenomena and demonstrates the reduction in membrane dehydration and GDL flooding that follow from the presence of an MPL.

Acknowledgements

This work was supported by a Korea Research Foundation Grant (KRF-2008-331-D00120) that was funded by the Korean Government (MOEHRD, Basic Research Promotion Fund). Thanks are also due to CD-adapco, Korea, for their technical support for STAR-CD licenses.

References

[1] Z. Qi, A. Kaufman, J. Power Sources 109 (2002) 38–46.
[2] M.S. Wilson, J.A. Valerio, S. Gottesfeld, Electrochim. Acta 40 (1995) 355–363.
[3] H.H. Voss, D.P. Wilkinson, P.G. Pickup, M.C. Johnson, V. Basura, Electrochim. Acta 40 (1995) 321–328.
[4] E. Passalacqua, F. Lufrano, G. Squadrito, A. Patti, L. Giorgi, Electrochim. Acta 43 (1998) 3665–3673.
[5] G.J.M. Janssen, M.L.J. Overvelde, J. Power Sources 101 (2001) 117–125.
[6] J. Chen, T. Matsuura, M. Hori, J. Power Sources 131 (2004) 155–161.
[7] C.S. Kong, D.Y. Kim, H.K. Lee, Y.G. Shul, T.H. Lee, J. Power Sources 108 (2002) 185–191.
[8] G.G. Park, Y.J. Sohn, T.H. Yang, Y.G. Yoon, W.Y. Lee, C.S. Kim, J. Power Sources 131 (2004) 182–187.
[9] X.L. Wang, H.M. Zhang, J.L. Zhang, H.F. Xu, Z.Q. Tian, J. Chen, H.X. Zhong, Y.M. Liang, B.L. Yi, Electrochim. Acta 51 (2006) 4909–4915.
[10] X.L. Wang, H.M. Zhang, J.L. Zhang, H.F. Xu, X. Zhu, J. Chen, B. Yi, J. Power Sources 162 (2006) 474–479.
[11] J. Chen, H. Xu, H. Zhang, B. Yi, J. Power Sources 182 (2008) 531–539.
[12] A.L. Ong, A. Bottino, G. Capannelli, A. Comite, J. Power Sources 183 (2008) 62–68.
[13] R.P. Ramasamy, E.C. Kumbur, M.M. Mench, W. Liu, D. Moore, M. Murthy, J. Power Sources 33 (2008) 3351–3367.
[14] H.K. Atiyeh, K. Karan, B. Peppley, A. Phoenix, E. Halliop, J. Pharoah, J. Power Sources 170 (2007) 111–121.
[15] F. Liu, C.Y. Wang, Electrochim. Acta 53 (2008) 5517–5522.
[16] J.H. Nam, M. Kaviany, Int. J. Heat Mass Transf. 46 (2003) 4595–4611.
[17] U. Pasaogullari, C.Y. Wang, Electrochim. Acta 49 (2004) 4359–4369.
[18] U. Pasaogullari, C.Y. Wang, K.S. Chen, J. Electrochem. Soc. 152 (8) (2005) A1574–A1582.
[19] A.Z. Weber, J. Newman, J. Electrochem. Soc. 152 (4) (2005) A677–A688.
[20] C.Y. Wang, P. Cheng, Int. J. Heat Mass Transf. 39 (1996) 3607–3618.
[21] H. Ju, G. Luo, C.Y. Wang, J. Electrochem. Soc. 154 (2) (2007) B218–B228.
[22] G. Luo, H. Ju, C.Y. Wang, J. Electrochem. Soc. 154 (3) (2007) B316–B321.
[23] H. Ju, J. Power Sources 191 (2009) 259–268.
[24] R.B. Bird, W.E. Stewart, E.N. Lightfood, Transport Phenomena, John Wiley & Sons, New York, 1960.
[25] CD-Adapco Group, STAR-CD Version 3.15 Methodology, USA, 2001.
[26] T.E. Springer, T.A. Zawodinski, S. Gottesfeld, J. Electrochem. Soc. 136 (1991) 2334–2341.